Stresses in constant tapered beams with thin-walled rectangular and circular cross sections

P. Bertolini[a], M.A. Eder[b], L. Taglialegne[c], P.S. Valvo[c]

[a]*LM Wind Power, Jupitervej 6, DK-6000 Kolding, Denmark, pbet@lmwindpower.com, corresponding author.*
[b]*Technical University of Denmark, Frederiksborgvej 399, DK-4000 Roskilde, Denmark, maed@dtu.dk*
[c]*Department of Civil and Industrial Engineering, University of Pisa, Largo Lucio Lazzarino, I-56122 Pisa, Italy, l.taglialegne@ing.unipi.it, p.valvo@ing.unipi.it*

Abstract

Tapered beams are widely employed in efficient flexure dominated structures. In this paper, analytical expressions are derived for the six Cauchy stress components in untwisted, straight, thin-walled beams with rectangular and circular cross sections characterised by constant taper and subjected to three cross-section forces. These expressions pertain to homogeneous, isotropic, linear elastic materials and small strains. In fact, taper not only alters stress magnitudes and distributions but also evokes stress components, which are zero in prismatic beams. A parametric study shows that increasing taper decreases the von Mises stress based fatigue life, suggesting that step-wise prismatic approximations entail non-conservative designs.

Keywords:
Tapered beams, thin-walled hollow sections, beam theory, analytical solution, isotropic material

Nomenclature

Symbol	Unit	Description
A	m^2	area of cross section
A^*	m^2	area of hatched cross section
b	m	half width of box girder cross section
b_r, b_θ, b_z	N/m^3	body forces in cylindrical coordinates
c	m	chord length

C		Basquin's constant
e	m	eccentricity
E	Pa	Young's modulus
F_y, F_z	N	shear and axial forces
F_y^L, F_z^L	N	shear and axial forces at $z = L$
F_y^0, F_z^0	N	shear and axial forces at $z = 0$
h	m	half height of box beam cross section
h_0	m	half height of box beam cross section at $z = 0$
I_x	m^4	second moment of area of cross section
J_2	Pa^2	second deviatoric invariant
L	m	beam length
m_x	N	distributed couple per unit length
M_x	Nm	bending moment
M_x^L	Nm	bending moment at $z = L$
M_x^0	Nm	bending moment at $z = 0$
n		Basquin's constant
N		number of cycles to failure
$\tilde{N}$		normalised number of cycles to failure (cone over cylinder)
O		origin of reference system
p_y, p_z	N/m	distributed loads per unit length
R	m	radius of conical beam cross section
R_0	m	radius of conical beam cross section at $z = 0$
$\mathbb{R}$		set of the real numbers
S_x^*	m^3	first moment of area of hatched cross section
t	m	thickness of conical beam wall
t_f	m	thickness of box beam flange
t_p	m	projected wall thickness
t_w	m	thickness of box beam web
V	m^3	volume
x, y, z		Cartesian coordinates
$1, 2, 3$		local reference axes
α	rad	angle of taper
η	m	local abscissa
θ	rad	polar angle
ν		Poisson's ratio
σ_{ij}	Pa	stress tensor components
σ_{vM}	Pa	equivalent von Mises stress

σ_{vM}^{norm}	normalised von Mises stress (cone over cylinder)
σ_{vM}^{α}	normalised von Mises stress (negative over positive angle)

1. Introduction

The reduction of mass and the consequent savings in manufacturing costs are an increasingly important and compelling aspect of structural optimisation. A well-established means to increase the stiffness-to-mass ratio of beam type structures is the introduction of lengthwise geometrical variations. The probably most widely employed expedient – in this paper denoted as *taper* – refers to a variation of the cross-section height and/or width along the beam axis according to the governing internal force distribution. Some prominent examples of tapered beams are bridge girders at intermediate supports, frame/truss structures for industrial halls and hangars, aircraft wings, wind turbine towers, and wind turbine rotor blades [1, 2, 3].

In a beam with a straight centreline and variable cross section, the *angle of taper*, α, can be defined as the angle enclosed by the local tangent plane to the beam lateral surface and the beam axis i.e. the lengthwise gradient of the lateral surface with respect to the beam axis. In general, the angle of taper will be a pointwise function. In the simplest case – herein referred to as *constant taper* – the angle of taper does not change along the beam axis [4].

It is well-known in literature that beams with variable cross sections show a significantly different behaviour in contrast to prismatic beams. Variable cross-section beams exhibit a non-trivial stress distribution in particular the shear stresses evoked are counter intuitive and hardly predictable by the classical theory for prismatic beams [5, 6].

The effects of taper on the shear stress distribution in simple planar non-prismatic beams were already investigated by Timoshenko [7]. Bleich [8] derived a closed-form solution showing that in tapered beams shear stresses are induced not only by shear forces, but also by axial forces and bending moments. Unfortunately, Bleich was misled by the analogy with prismatic beams and referred to the centreline as the locus of maximum shear stresses. Later, Paglietti and Carta [9] demonstrated that the maximum shear stress does not necessarily occur at the elastic centre of the cross-section.

Atkin proposed a different approach based on classical elasticity, defining proper stress functions for specific aeronautical problems [10, 11]. Subsequently, Krahula [12] compared the predictions of Bleich's formula – even

3

though not citing directly [8] but referring to Timoshenko and Gere [13] – and the solution of a two-dimensional elasticity problem for a tapered cantilever beam loaded by a concentrated shear force at its free end. Elasticity theory has been used to model tapered beams also by Knops and Villaggio [14], and more recently by Trahair and Ansourian [15].

The behaviour of tapered beams under bending and torsion was extensively investigated by Lee and Szabo [16] and Lee et al. [17].

Chong et al. [18] showed by means of simplified mechanical models that the shear stress in the webs of I- and box girders strongly depends on both the sign of the taper, i.e. the positive or negative slope, and the direction of the shear force.

With the rise of structural optimisation in the past decades, research increasingly focused on the development of computationally efficient semi-analytical numerical methods for tapered elastic 2D beams with solid rectangular cross sections. Hodges et al. [19, 20] and Rajagopal [21] developed the variational-asymptotic method, which is capable of providing a full elasticity solution in terms of stresses, strains, and displacements for 2D beams with constant taper subjected to shear and axial forces, and bending moments. Balduzzi et al. [22] derived a non-prismatic planar beam element from a 2D elastic solution. More recently, Balduzzi et al. [23] extended the approach also to multilayer planar non-prismatic beams.

Taglialegne [6] derived an exact analytical elastic solution for a tapered planar beam subject to shear and axial forces, and bending moment based on the solution of the wedge proposed by Michell [24] and Carothers [25]. Bennati et al. [4, 26] showed that the shear stress distribution – also numerically predicted by Balduzzi et al. [22] – may be a satisfactory approximation of the exact solution.

It is noteworthy to mention that the optimisation of tapered beams comprising of complex thin-walled single- or multi-cellular hollow sections gained a lot of attention, especially in the industry. Topology optimisation techniques rely on computationally efficient stress analysis tools which usually exclude the use of computationally demanding 3D finite element models. As a remedy, the so-called cross-sectional analysis tools, such as BECAS [27] and VABS [28], have been developed for the efficient analysis of slender beam-type structures. However, many cross-sectional analysis tools as well as beam elements intended for the use of modelling tapered hollow sections approximate the tapered beams to step-wise prismatic beams.

This paper provides analytical expressions for the six Cauchy stress ten-

4

sor components occurring in tapered beams with thin-walled rectangular and circular cross-sections, shortly referred to in the following as *tapered box beam* and *thin-walled conical beam*, respectively. The derivation is carried out in the hypothesis of homogeneous, isotropic, linear elastic material behaviour and first-order Euler-Bernoulli beam theory. First, an extension of Jourawski's formula for shear stresses is deduced for straight and untwisted beams with doubly-symmetric variable cross sections, subjected to distributed loads producing axial force, shear forces, and bending moment (in a symmetry plane of the cross section). The deduction assumes that Navier's formula yields a good approximation of the normal stresses in variable cross-section beams with moderate taper angles. (for a deeper discussion of this issue the reader is referred to Boley [29]). Subsequently, the extended Jourawski's formula is specialised to the tapered box beam and thin-walled conical beam, under the assumed absence of distributed loads. The remaining stress components are obtained through the assumption of plane stress in the thin cross-section walls by integration of the Cauchy equilibrium differential equations.

The analytical solutions are validated against 3D finite element analyses for constant-taper cantilever beams clamped at one end (the *root* section) and loaded at the free end (the *tip* section). The numerical results show that already small taper angles (in the order of few degrees) not only considerably alter the stress distributions obtained from prismatic beam theory, but can evoke stress components which are zero otherwise. The potential implications of the effects of taper on beam designs have to date not been investigated to the best knowledge of the authors. Therefore, the analytically derived solutions were used in a comprehensive parametric study to shed light on the effect of constant taper on the von Mises stress and consequently on the fatigue life of thin-walled conical beams.

2. Analytical solution

2.1. Extended shear formula

A variable cross-section beam of length L, having a straight centreline and a doubly symmetric cross section (Fig. 1) is considered. A global Cartesian reference system $Oxyz$ is fixed with the origin O located in the centre of one of the end sections; the x- and y-axes are aligned with the principal cross-section axes of inertia (coincident with the symmetry axes) where the z-axis is coincident with the beam centreline. Here, it is stipulated that the beam is
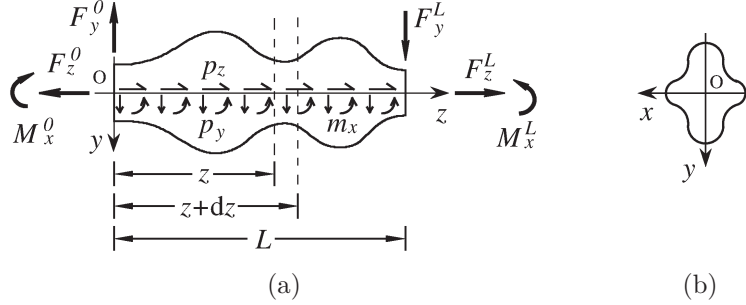
Figure 1: (a) Beam with variable cross section subjected to distributed axial and transverse loads, and bending couple. (b) Generic cross section with two axes of symmetry.

not twisted, i.e. that the principal directions of inertia of each cross section are parallel to the x- and y-axes.

The beam is subjected to distributed loads, $p_y(z)$ and $p_z(z)$, acting in the y- and z-directions, respectively, and to a distributed bending couple, $m_x(z)$. With the above assumptions, the internal forces acting on each cross section will be the shear force, $F_y(z)$, axial force, $F_z(z)$, and bending moment, $M_x(z)$. Local equilibrium demands that:

$$\frac{\mathrm{d}F_z(z)}{\mathrm{d}z} + p_z(z) = 0, \qquad \frac{\mathrm{d}F_y(z)}{\mathrm{d}z} + p_y(z) = 0, \qquad \frac{\mathrm{d}M_x(z)}{\mathrm{d}z} + m_x(z) = F_y(z) \tag{1}$$
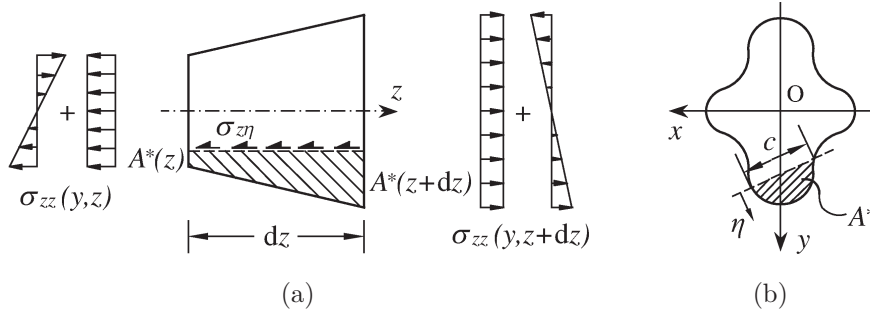

Figure 2: (a) Infinitesimal beam segment of length $\mathrm{d}z$. (b) Cross section with generic chord of length b and local abscissa η.

Global equilibrium of the beam requires also concentrated forces $F_y^0 = F_y(0)$, $F_z^0 = F_z(0)$, and $M_x^0 = M_x(0)$ to be applied at $z = 0$ and $F_y^L = F_y(L)$,

6

$F_z^L = F_z(L)$, and $M_x^L = M_x(L)$ at $z = L$.

In a prismatic beam, under the assumptions that plane cross sections remain plane after deformation and that the material is homogeneous, isotropic, and linearly elastic [30], Navier's formula furnishes the normal stresses on cross sections notably:

$$\sigma_{zz} = \frac{F_z}{A} + \frac{M_x}{I_x}y \tag{2}$$

where A and I_x respectively are the area and second moment of area with respect to the x-axis of the cross section. Here and in the following, the dependency upon z will be omitted if not strictly necessary.

Here, it is assumed that Navier's Eq. (2) holds also for beams of variable cross section. The validity of this assumption has been investigated by Boley [29], where a good approximation is obtained for moderate taper angles: for example, if $\alpha = 10$ deg, the error is around 7.5%.

Firstly, the infinitesimal segment of a variable cross-section beam slice between two cross sections located at z and $z + dz$ as shown in Fig. 1(a), is considered. Figure 2(a) illustrates the uniform and linearly variable normal stress distributions respectively induced by the axial force and bending moment acting on the infinitesimal beam segment. Secondly, a generic straight chord of length c is introduced, which subdivides the cross section into two complementary parts. Furthermore, a local abscissa denoted as η aligned orthogonal to the chord direction is introduced as shown in Fig. 2(b). Consequently, the infinitesimal beam segment itself turns out to be subdivided into two parts. The ensuing focus is put on the 'hatched' part associated with the side of positive η. The corresponding cross-section area is denoted as A^*.

In order to determine an expression for the shear stresses acting on the cross section in the direction orthogonal to the chord, $\sigma_{z\eta}$, the equilibrium of the 'hatched' part of the beam segment is imposed depicted in Fig. 3. Assuming that the axial loads, p_z, are uniformly distributed on the cross section, the equilibrium in the z-direction can be written as:

$$\int\limits_{A^*(z)} \sigma_{zz}\, dA + \sigma_{z\eta} \frac{c + (c + dc)}{2}\, dz - \int\limits_{z}^{z+dz} \int\limits_{A^*(z)} \frac{p_z}{A}\, dA\, dz = \int\limits_{A^*(z+dz)} (\sigma_{zz} + d\sigma_{zz})\, dA \tag{3}$$

Following Taglialegne [6], Eq. (3) can be expanded and higher-order

7

infinitesimal terms neglected. Hence,

$$\sigma_{z\eta} = \frac{1}{c} \int_{A^*} \frac{d\sigma_{zz}}{dz} \, dA + \frac{1}{c} \frac{p_z}{A} \int_{A^*} dA \qquad (4)$$

Figure 3: Equilibrium in the z-direction of the 'hatched' part of the infinitesimal beam segment of length dz

By substituting Eqs. (1) and (2) into (4), after simplification, the general solution for the cross-section shear stress component is obtained:

$$\sigma_{z\eta} = \frac{1}{c} \left[F_z \frac{d}{dz} \left(\frac{A^*}{A} \right) + (F_y - m_x) \frac{S_x^*}{I_x} + M_x \frac{d}{dz} \left(\frac{S_x^*}{I_x} \right) \right] \qquad (5)$$

where S_x^* is the first moment of area of the 'hatched' part of the cross section with respect to the x-axis.

It is worth noting that Eq. (5) can be considered as a generalisation of a similar formula derived by Bleich [8] for a beam with constant width and variable height for the specific case that $dF_z/dz = 0$.

2.2. Vertically tapered box beam

The extended shear formula Eq. (5) can be specialised to the vertically tapered box beam shown in Fig. 4. The cantilever beam studied in this paper is exemplary. However, the assumed support conditions do not pose any restriction to the validity of these specialised equations. The cross-section width, $2b$, is constant, while the cross-section height, $2h(z)$, varies linearly with the z-coordinate according to:

$$h(z) = h_0 - z \tan \alpha \qquad (6)$$

where h_0 denotes the half height of the root section and α is the angle of taper. The thicknesses of the flanges, t_f, and webs, t_w, are assumed to be

constant along the z-coordinate and small with respect to the cross-section dimensions. According to the defined geometry, the Cartesian coordinates of the thin wall mid-surface vary within the following limits:

$$x \in [-b,\, b] \subseteq \mathbb{R} \tag{7}$$

$$y \in [-h(z),\, h(z)] \subseteq \mathbb{R} \tag{8}$$

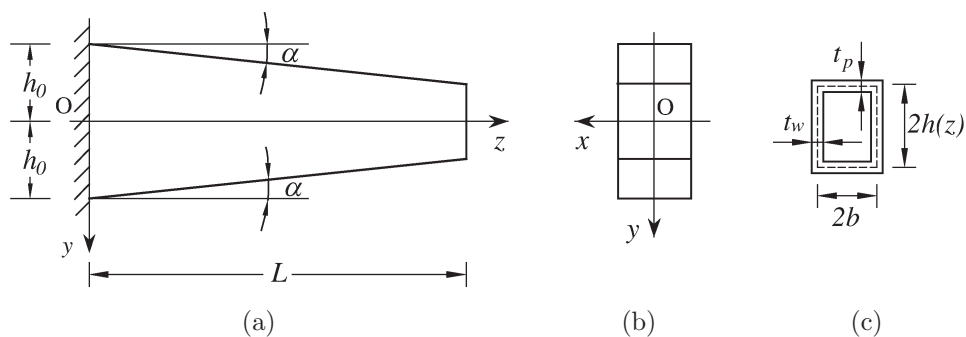$$z \in [0,\, L] \subseteq \mathbb{R} \tag{9}$$

Figure 4: (a) Side and (b) front views of a thin-walled vertically tapered cantilever box beam of length L and taper angle α. (c) Arbitrary cross section, where the projected flange thickness, t_p, and web thickness, t_w, are highlighted.

The flange thickness projected in the cross-section plane is

$$t_p = \frac{t_f}{\cos \alpha} \tag{10}$$

Hence, the cross-section area and second moment of area with respect to the x-axis are respectively:

$$A = 4 \left[b\, t_p + t_w\, h(z) \right] \tag{11}$$

$$I_x = 4 \left[b\, t_p\, h(z)^2 + \frac{1}{3} t_w h(z)^3 \right] \tag{12}$$

Utilising symmetry, the solution can be reduced to a quarter of the cross section. In what follows, the stress fields are evaluated separately in the half flange and half web of the positive quadrant, $x \geq 0$ and $y \geq 0$.

9

2.2.1. Stress components in the flange

The half flange defined by $0 \leq x \leq b$ and $y = h(z)$ is considered. Here, the normal stress component is directly determined by substituting Eq. (11) and (12) into (2):

$$\sigma_{zz}^f = \frac{1}{4} \left[\frac{F_z}{b\, t_p + t_w\, h(z)} + \frac{3M_x}{3b\, t_p\, h(z) + t_w\, h(z)^2} \right] \tag{13}$$
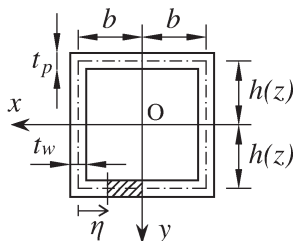
Figure 5: Hatched portion of cross section on the flange.

The area and first moment of area with respect to the x-axis of the 'hatched' portion of cross section on the flange (see Fig. 5) with $\eta = b - x$, can be written as follows:

$$A^* = x\, t_p \tag{14}$$
$$S_x^* = x\, t_p\, h(z) \tag{15}$$

Subsequently, by substituting Eqs. (11), (12), (14), and (15) into (5), with $c = t_p$, the shear stress component on the flange is obtained:

$$
\sigma_{zx}^f = -\frac{1}{4}x \left\{ \frac{F_z\, t_w \tan\alpha}{[b\, t_p + t_w\, h(z)]^2} + \frac{3F_y}{3b\, t_p\, h(z) + t_w\, h(z)^2} \right.
$$
$$
\left. + \frac{3M_x \tan\alpha\, [3b\, t_p + 2t_w\, h(z)]}{h(z)^2\, [3b\, t_p + t_w\, h(z)]^2} \right\}. \tag{16}
$$

To determine the remaining stress components, first a local coordinate system 123 is defined such that the 2-axis is parallel to the x-axis and the 3-axis is the outward normal to the flange as illustrated in Fig. 6.
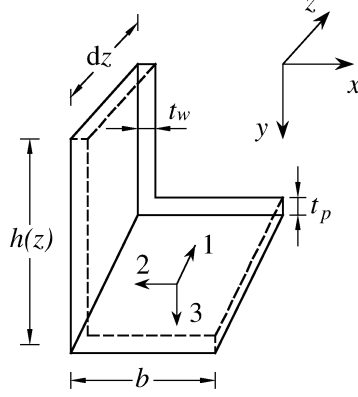
Figure 6: Quarter of an infinitesimal segment of the vertically tapered box beam with global, xyz, and local, 123, reference systems.

The stress components in the local and global reference systems can be related by introducing a rotation matrix as follows:

$$
\begin{bmatrix} \sigma_{11}^f & \sigma_{12}^f & \sigma_{13}^f \\ \sigma_{21}^f & \sigma_{22}^f & \sigma_{23}^f \\ \sigma_{31}^f & \sigma_{32}^f & \sigma_{33}^f \end{bmatrix} = \begin{bmatrix} 0 & -\sin\alpha & \cos\alpha \\ 1 & 0 & 0 \\ 0 & \cos\alpha & \sin\alpha \end{bmatrix} \begin{bmatrix} \sigma_{xx}^f & \sigma_{xy}^f & \sigma_{xz}^f \\ \sigma_{yx}^f & \sigma_{yy}^f & \sigma_{yz}^f \\ \sigma_{zx}^f & \sigma_{zy}^f & \sigma_{zz}^f \end{bmatrix} \begin{bmatrix} 0 & 1 & 0 \\ -\sin\alpha & 0 & \cos\alpha \\ \cos\alpha & 0 & \sin\alpha \end{bmatrix}
\tag{17}
$$

Accordingly, under the assumption of a plane stress state in the flange, the local stress component condition $\sigma_{31}^f = \sigma_{32}^f = \sigma_{33}^f = 0$ must hold. Consequently, Eqs. (17) yield:

$$
\sigma_{yy}^f = \sigma_{zz}^f \tan^2\alpha
\tag{18}
$$

$$
\sigma_{xy}^f = -\sigma_{zx}^f \tan\alpha
\tag{19}
$$

$$
\sigma_{yz}^f = -\sigma_{zz}^f \tan\alpha
\tag{20}
$$

The last unknown stress component is obtained by integrating the first Cauchy equilibrium equation, Eq. (A.1):

$$
\sigma_{xx}^f = -\int_0^x \frac{\partial \sigma_{zx}^f}{\partial z}\,\mathrm{d}x + \sigma_{xx}^f\big|_{x=b}
\tag{21}
$$

where $\sigma_{xx}^f\big|_{x=0}$ represents an integration constant which can be determined after deduction of the solution for the stresses in the web.

11

2.2.2. Stress components in the web

In the following the half web, defined by $x = b$ and $0 \leq y \leq h(z)$, is considered. The normal stress component is directly determined by substituting Eq. (11) and (12) into (2):

$$\sigma_{zz}^w = \frac{1}{4} \left[\frac{F_z}{b\,t_p + t_w\,h(z)} + \frac{3M_x\,y}{3b\,t_p\,h(z)^2 + t_w\,h(z)^3} \right] \tag{22}$$
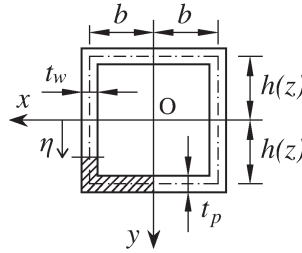

Figure 7: Hatched portion of cross section on the web

On the web, the 'hatched' portion of cross section includes the half flange and a part of the web, with $\eta = y$, as illustrated in Fig. 7. The area and moment of inertia with respect to the x-axis are respectively:

$$A^* = b\,t_p + t_w\,[h(z) - y] \tag{23}$$

$$S_x^* = b\,t_p\,h(z) + \frac{t_w}{2} \left[h(z)^2 - y^2 \right] \tag{24}$$

By substituting Eqs. (11), (12), (23), and (24) into (5), with $c = t_w$, the shear stress component on the web is obtained as follows:

$$
\begin{aligned}
\sigma_{yz}^w = {} & -\frac{F_z}{4} \frac{t_w\,y\,\tan\alpha}{[b\,t_p + t_w\,h(z)]^2} + \frac{3F_y}{8\,t_w} \frac{2b\,t_p\,h(z) + t_w\,[h(z)^2 - y^2]}{h(z)^2\,[3b\,t_p + t_w\,h(z)]} \\
& + \frac{3\,M_x}{8\,t_w} \frac{\tan\alpha}{[3b\,t_p + t_w\,h(z)]^2\,h(z)^3} \\
& \left\{ 6b^2\,t_p^2\,h(z) + 2b\,t_p\,t_w\,[2h(z)^2 - 3y^2] + t_w^2\,h(z)\,[h(z)^2 - 3y^2] \right\}
\end{aligned}
\tag{25}
$$

The webs are assumed to be in a plane-stress state. Consequently, $\sigma_{xx}^w = \sigma_{xy}^w = \sigma_{xz}^w = 0$. The last unknown stress component is obtained by integration

12

of the second Cauchy equilibrium equation, Eq. (A.2):

$$\sigma_{yy}^w = -\int_0^y \frac{\partial \sigma_{yz}^w}{\partial z}\, \mathrm{d}y + \sigma_{yy}^w\big|_{y=h} \tag{26}$$

where $\sigma_{yy}^w\big|_{y=0}$ is an integration constant.

2.2.3. Equilibrium conditions on edges

The solution for the stress distribution in the box beam is already completely determined, except for the two integration constants, $\sigma_{xx}^f\big|_{x=0}$ and $\sigma_{yy}^w\big|_{y=0}$. The latter can be calculated by imposing the equilibrium of an infinitesimal edge portion of length $\mathrm{d}z$ connecting the flange and web as shown in Fig. 8. Neglecting higher-order infinitesimal terms, equilibrium in the x-direction gives:

$$t_f\ \sigma_{xx}^f\big|_{x=b}\ \frac{\mathrm{d}z}{\cos\alpha} + t_w\ \sigma_{xy}^w\big|_{y=h}\ \mathrm{d}z + t_w\ \sigma_{zx}^w\big|_{y=h}\ \tan\alpha\ \mathrm{d}z = 0 \tag{27}$$

and equilibrium in the y-direction gives:

$$t_f\ \sigma_{xy}^f\big|_{x=b}\ \frac{\mathrm{d}z}{\cos\alpha} + t_w\ \sigma_{yy}^w\big|_{y=h}\ \mathrm{d}z + t_w\ \sigma_{yz}^w\big|_{y=h}\ \tan\alpha\ \mathrm{d}z = 0. \tag{28}$$
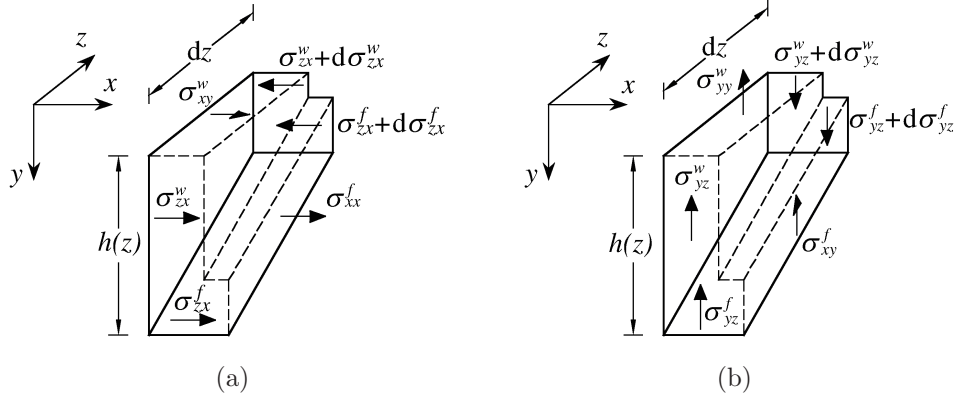
Figure 8: Stresses acting in the (a) x- and (b) y-directions on an infinitesimal edge portion between the flange and web of the box beam.

13

By substituting Eqs. (21) and (26) into (27) and (28) respectively, results in:

$$\sigma_{xx}^f = \int_0^b \frac{\partial \sigma_{zx}^f}{\partial z} \, dx - \frac{t_w}{t_f} \left(\cos \alpha \, \sigma_{xy}^w|_{y=h} + \sin \alpha \, \sigma_{zx}^w|_{y=h} \right) \tag{29}$$

$$\sigma_{yy}^w = \int_0^h \frac{\partial \sigma_{yz}^w}{\partial z} \, dy - \tan \alpha \, \sigma_{yz}^w|_{y=h} - \frac{t_f}{t_w \cos \alpha} \sigma_{xy}^f|_{x=b} \tag{30}$$

Due to the complexity of the mathematical expressions involved, it is convenient to solve Eqs. (29) and (30) numerically at each cross section to determine the values of the integration constants and complete the determination of the stress distribution in the beam.

2.3. Thin-walled conical beam

Figure 9 shows a thin-walled conical cantilever beam. The radius defining the wall mid-surface can be written as:

$$R(z) = R_0 - z \tan \alpha \tag{31}$$

where α is the taper angle and R_0 is the root radius. The polar angle, θ, is assumed counterclockwise from the x-axis.
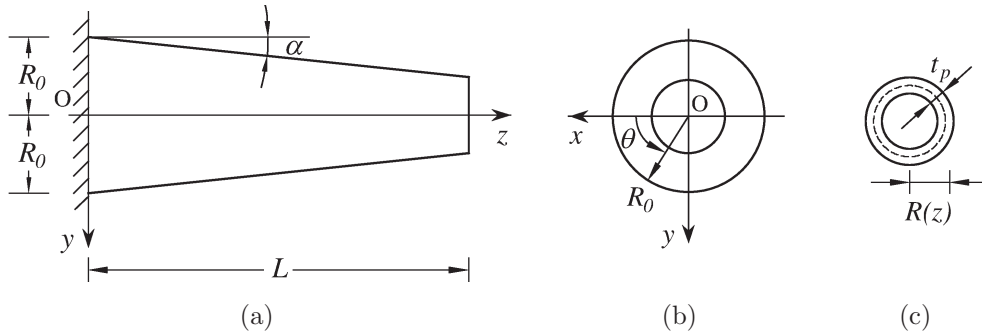
Figure 9: (a) Side and (b) frontal views of a thin-walled conical cantilever beam of length L and taper angle α. (c) Arbitrary cross section, where the projected wall thickness t_p is highlighted.

The wall thickness, t, is assumed to be constant with the z-coordinate and small with respect to the cross-section radius. The projected wall thickness,

cross-sectional area and second moment of area with respect to the x-axis respectively are:

$$t_p = \frac{t}{\cos \alpha} \tag{32}$$

$$A = 2\pi t_p R(z) \tag{33}$$

$$I_x = 2 \int_0^\pi t_p \sin^2 \theta R^3(z) \, \mathrm{d}\theta = \pi t_p R^3(z) \tag{34}$$

The normal stress on the cross section is directly obtained by substituting Eqs. (33) and (34) into (2) with $y = \sin \theta R(z)$:

$$\sigma_{zz} = F_z \frac{\cos \alpha}{2\pi t R(z)} + M_x \frac{\cos \alpha \sin \theta}{\pi t R(z)^2} \tag{35}$$
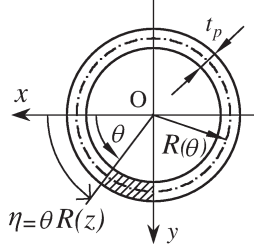
Figure 10: Hatched portion of conical cross section

The area and first moment of area of the 'hatched' part of the conical cross section defined by $\eta = \theta R(z)$ and illustrated in Fig. 10, are respectively given by:

$$A^* = \int_\theta^{\pi/2} t_p R(z) \, \mathrm{d}\theta = (\pi - \theta) t_p R(z) \tag{36}$$

$$S_x^* = \int_\theta^{\pi/2} t_p \sin \theta R^2(z) \, \mathrm{d}\theta = t_p \cos \theta R^2(z) \tag{37}$$

The circumferential shear stress is determined by substituting Eqs. (33), (34), (36), and (37) into (5), with $c = t_p$:

$$\sigma_{z\theta} = F_y \frac{\cos \alpha \cos \theta}{\pi t R(z)} + M_x \frac{\sin \alpha \cos \theta}{\pi t R(z)^2} \tag{38}$$

15

Figure 11 shows the three different coordinate systems (CSYS) defined in a conical beam segment: the global CSYS, xyz, the cylindrical CSYS, $r\theta z$, and the local CSYS, 123. The latter is oriented such that the 12-plane is tangent to the thin wall mid-surface with the 2-axis opposite to θ and with the 3-axis pointing in the outer normal direction.
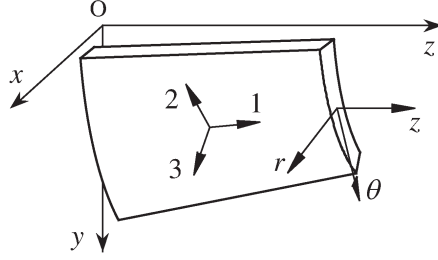

Figure 11: Global coordinates x, y, z, cylindrical coordinates r, θ, z, and local coordinates $1, 2, 3$ in a conical beam.

Thus, the stress tensor components in the cylindrical and local reference systems can be related as follows:

$$
\begin{bmatrix} \sigma_{rr} & \sigma_{r\theta} & \sigma_{rz} \\ \sigma_{\theta r} & \sigma_{\theta\theta} & \sigma_{\theta z} \\ \sigma_{zr} & \sigma_{z\theta} & \sigma_{zz} \end{bmatrix} = \begin{bmatrix} -\sin\alpha & 0 & \cos\alpha \\ 0 & -1 & 0 \\ \cos\alpha & 0 & \sin\alpha \end{bmatrix} \begin{bmatrix} \sigma_{11} & \sigma_{12} & \sigma_{13} \\ \sigma_{21} & \sigma_{22} & \sigma_{23} \\ \sigma_{31} & \sigma_{32} & \sigma_{33} \end{bmatrix} \begin{bmatrix} -\sin\alpha & 0 & \cos\alpha \\ 0 & -1 & 0 \\ \cos\alpha & 0 & \sin\alpha \end{bmatrix}^T
$$
(39)

Under the assumption of plane stress in the wall, the local stress components σ_{31}, σ_{32}, and σ_{33} are identically null. Consequently, Eqs. (39) produce a set of three linear equations for the unknowns σ_{rr}, $\sigma_{r\theta}$, and σ_{rz}:

$$
\begin{cases} \sigma_{31} = 2\sigma_{zr}\cos 2\alpha - (\sigma_{rr} - \sigma_{zz})\sin 2\alpha = 0 \\ \sigma_{32} = \sigma_{r\theta}\cos\alpha + \sigma_{\theta z}\sin\alpha = 0 \\ \sigma_{33} = \sigma_{rr}\cos^2\alpha + \sigma_{zr}\sin 2\alpha + \sigma_{zz}\sin^2\alpha = 0 \end{cases}
$$
(40)

The solution of the linear set of equations is:

$$
\sigma_{rr} = \sigma_{zz}\tan^2\alpha
$$
(41)

$$
\sigma_{r\theta} = -\sigma_{\theta z}\tan\alpha
$$
(42)

$$
\sigma_{zr} = -\sigma_{zz}\tan\alpha
$$
(43)

16

Finally, the hoop stress component, $\sigma_{\theta\theta}$, is immediately derived from the first of the local equilibrium equations for a hollow thin conical element, whose derivation is presented in Appendix A. Substituting Eqs. (43) and (42) into (B.5) leads to $\sigma_{\theta\theta} = 0$ for all the loading conditions considered.

3. Numerical analysis

The analytical solutions of the two described geometries were compared with finite element models for verification. Two cantilever beams, namely the *rectangular beam* and the *conical beam*, were modelled inside the commercial finite element package Abaqus 2017 [31]. The mesh topology of these models is depicted in Fig. 12.

A control section perpendicular to the beam z-axis at the mid-span cross section was used for validation. Following Saint-Venant's principle the control section was chosen sufficiently far away from the root and tip sections in order to avoid boundary effects affecting the far-field solutions derived. The geometrical properties of the two models are listed in Table 1.

Table 1: Geometrical properties of the rectangular and conical beam models.

	Beam					Mid-span cross section		
	L	α	t_f	t_w	t	$2\,h$	$2\,b$	$2\,R$
	[m]	[deg]	[mm]	[mm]	[mm]	[m]	[m]	[m]
Rectangular	10.0	4.0	10.0	10.0	-	1.0	1.0	-
Conical	10.0	4.0	-	-	10.0	-	-	1.0

Homogeneous, isotropic, linear elastic material properties for steel were assigned with an elastic modulus of $E = 210\,\text{GPa}$ and a Poisson's ratio of $\nu = 0.3$. The models were discretized by enriched eight-noded solid elements (Abaqus element type C3D8R) as given by Tab. 2. The wall was discretised with two elements through the thickness.

A convergence study of different mesh densities was performed and the numerical results presented are obtained from sufficiently discretized models.

The kinematic (rigid) coupling constraints applied to the nodes of both ends of the beam, were coupled to a master node located in the elastic centre of the cross sections. The model was loaded at the master node located at the tip through application of concentrated forces, F_y^L, F_z^L, and/or bending moment, M_x^L. Table 3 lists the single load cases used in this study. All six

Table 2: Mesh discretisation and model size parameters of the two numerical models. The fourth and fifth columns refer to the largest and smallest transverse element sizes measured in the cross-section plane. The rectangular model has a higher mesh density because of the higher resolution required at the corners.

	# of el.	# of nodes	max el. size [m]	min el. size [m]
Rectangular	134 400	202 104	49.25×10^{-3}	5.00×10^{-3}
Conical	128 000	216 720	27.14×10^{-3}	5.43×10^{-3}

(a)   (b)
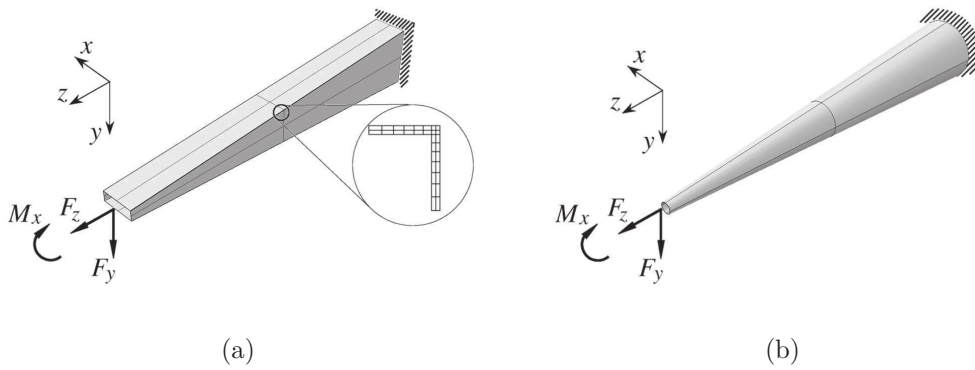
Figure 12: 3D finite element model of (a) the tapered rectangular beam, and (b) the cone. In both figures the loads and the boundary conditions are applied at a reference point, which is linked through a rigid coupling constraint to the tip or root cross section. In Figure (a) the detail of the mesh refinement at the corner is illustrated.

degrees of freedom of the master node of the root section were restrained such that the beam was fully clamped. A direct solution strategy was used (Abaqus linear perturbation). Results were extracted in global coordinates along node-paths located in the wall mid-surface at the control cross section.

4. Results

4.1. Stress analysis

The six components of the stress field produced by the axial and shear loads, and bending moment were evaluated via both the analytical solutions derived in Section 2 and the numerical finite element analysis for the two geometries previously described. Because of symmetry in the x and y direction, the stresses were evaluated along the center line of a quarter of the

Table 3: Load cases applied to both models in order to investigate the effect of taper under shear-bending, pure axial force and pure bending, and cross-section forces at mid-span. The applied bending moment is comparable to the resulting shear bending.

Case	Tip loads			Internal forces at the mid-span		
	F_y [N]	F_z [N]	M_x [N m]	F_y [N]	F_z [N]	M_x [N m]
Shear	1000	-	-	1000	-	-5000
Extension	-	1000	-	-	1000	-
Bending	-	-	5000	-	-	5000

control cross section. In Figures 13 - 20, the label *An* indicates the stresses evaluated through the analytical solutions, whereas the label *Num* indicates the FE results. Moreover, the deviation between the numerical and the analytical results is given by the *Normalised Mean Square Error* (NMSE) [32] in Tables 4, 5, and 6.

4.1.1. Vertically tapered box beam

The plots concerning the rectangular beams show the stresses evaluated along the mid-surface of half flange $(0 \leq x \leq b)$ and half web $(0 \leq y \leq h)$. Figures 13, 15, and 14 depict the stresses distribution along the flange, while Fig. 16 and 17 along the web. The stress components σ_{xx}, σ_{xy}, and σ_{xz} are zero along the web and have therefore been omitted. The stress singularity induced by the sharp corner in the FE models can be noted in Figs. 15, 14, and 16 when x and y approach $0.5\,\mathrm{m}$. The singularity effect of the corner is not considered in the analytical expressions which explains the deviations between the latter and the numerical predictions when approaching the corner.

4.1.2. Thin-walled conical beam

Figures 18, 19 and 20 compare the five analytically and numerically obtained stress components in cylindrical coordinates. The stresses were evaluated in the first quadrant, $0 \leq \theta \leq \pi/2$, utilising the cross section symmetry. Moreover, the numerical stress field was extracted after transformation from global Cartesian to cylindrical coordinates in Abaqus. The numerical results of the hoop stress component are not reported, since it is equal to zero along the cross section wall.
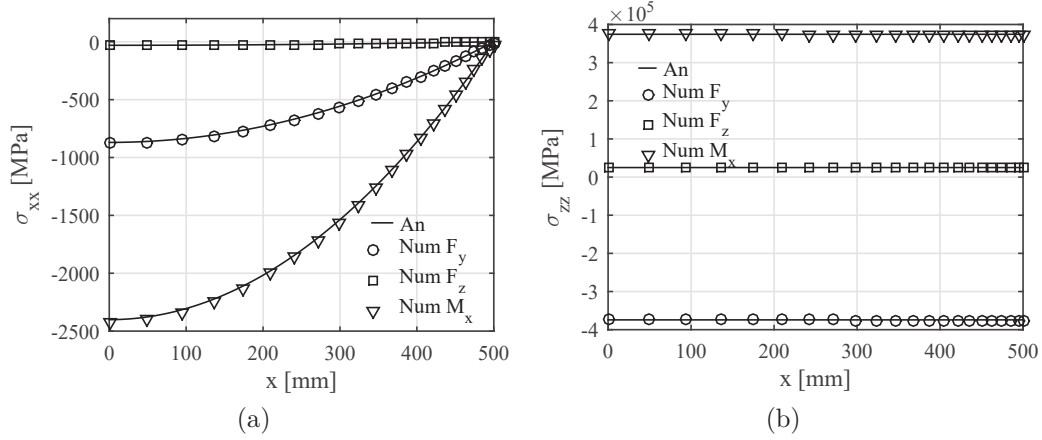
Figure 13: (a) σ_{xx} and (b) σ_{zz} stress distributions along the flange.
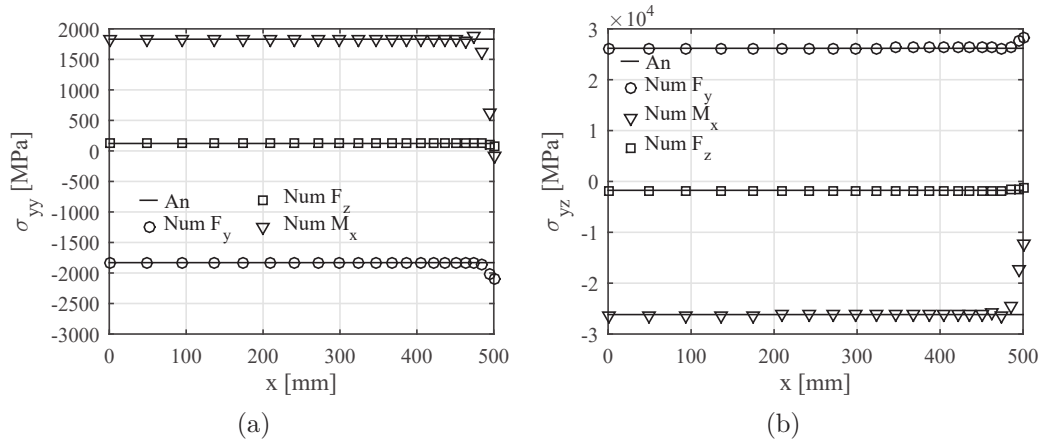

Figure 14: (a) σ_{yy} and (b) σ_{yz} stress distributions along the flange.

4.2. Parametric study

In order to highlight the impact of the taper on design applications, a parametric study of the taper affecting the equivalent stress of a beam under different loads condition is presented. Since a linear isotropic material is considered, the equivalent stress is evaluated through the von Mises criterion, $\sigma_{vM} = \sqrt{3\,J_2}$, where J_2 is the second deviatoric stress invariant [13]. It considers all stress components and it is invariant with respect to rotation of the coordinates system: in this way the global stress tensor could directly
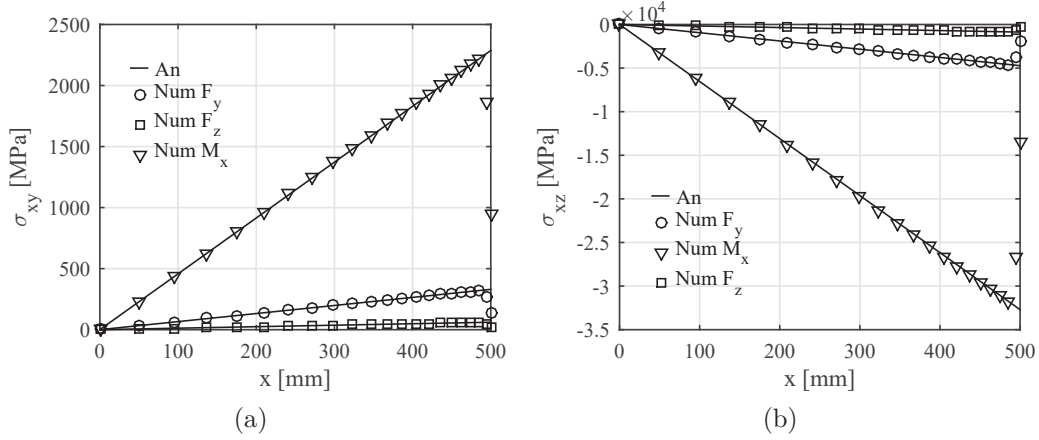
Figure 15: (a) σ_{xy} and (b) σ_{xz} stress distributions along the flange.

Table 4: *NMSE* along the flange of a vertically tapered beam. It was evaluated after excluding the three points closer to the cross section corner, where a singularity occurs.

Flange	σ_{xx}	σ_{xy}	σ_{xz}
F_z	1.31×10^{-5}	6.76×10^{-6}	7.33×10^{-6}
F_y	1.35×10^{-4}	7.43×10^{-5}	7.47×10^{-5}
M_x	9.88×10^{-5}	7.70×10^{-5}	1.85×10^{-5}
	σ_{xx}	σ_{xy}	σ_{xz}
F_z	2.77×10^{-5}	9.66×10^{-5}	2.61×10^{-6}
F_y	1.05×10^{-5}	2.00×10^{-5}	5.92×10^{-6}
M_x	1.75×10^{-4}	5.91×10^{-4}	1.65×10^{-5}

Table 5: *NMSE* along the web of a vertically tapered beam. It was evaluated after excluding the three points closer to the cross section corner, where a singularity occurs.

Web	σ_{zz}	σ_{yz}	σ_{yy}
F_z	1.11×10^{-5}	7.37×10^{-6}	1.84×10^{-4}
F_y	4.30×10^{-6}	1.32×10^{-6}	2.16×10^{-6}
M_x	3.80×10^{-5}	1.44×10^{-5}	2.31×10^{-5}

be used without the necessity of transformation into the local material stress tensor. The parametric study compares a thin-walled cylinder of radius $2\,R = 1\,\mathrm{m}$ to a set of thin-walled cones having a fixed control section of radius
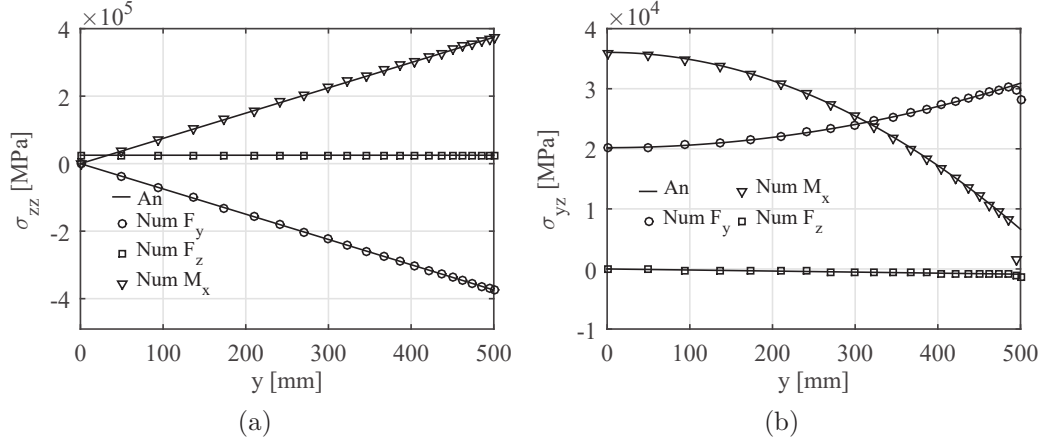
21

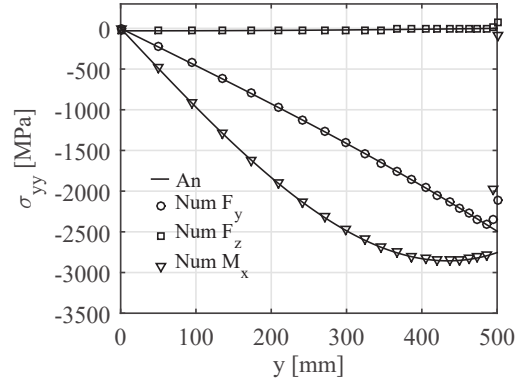Figure 16: (a) σ_{zz} and (b) σ_{yz} distributions along the web.

Figure 17: σ_{yy} stress distribution along the web.

Table 6: *NMSE* along a quarter of a conical beam.

	σ_{zz}	σ_{rz}	$\sigma_{z\theta}$	$\sigma_{r\theta}$	σ_{rr}
F_z	1.31×10^{-5}	4.07×10^{-6}	–	–	1.97×10^{-6}
F_y	2.70×10^{-3}	2.79×10^{-3}	3.08×10^{-3}	3.06×10^{-3}	2.85×10^{-3}
M_x	2.70×10^{-3}	2.58×10^{-3}	2.56×10^{-3}	2.56×10^{-4}	1.97×10^{-6}

$2\,R = 1\,\text{m}$. The loads are introduced through the eccentricity, which is defined as the ratio between the bending moment and the shear force at the cross section. The study also includes cones with negative taper, as the

22
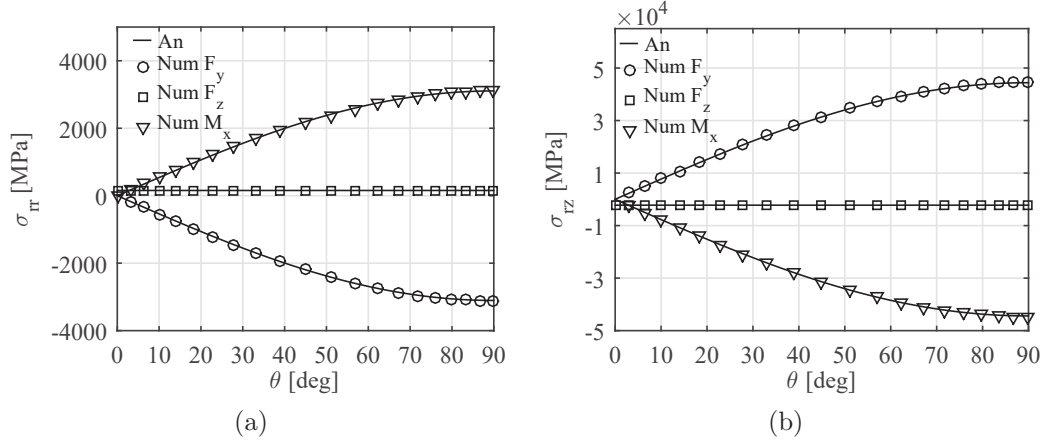
Figure 18: (a)σ_{rz} and (b) σ_{rr} stress distributions along a quarter of a cone.
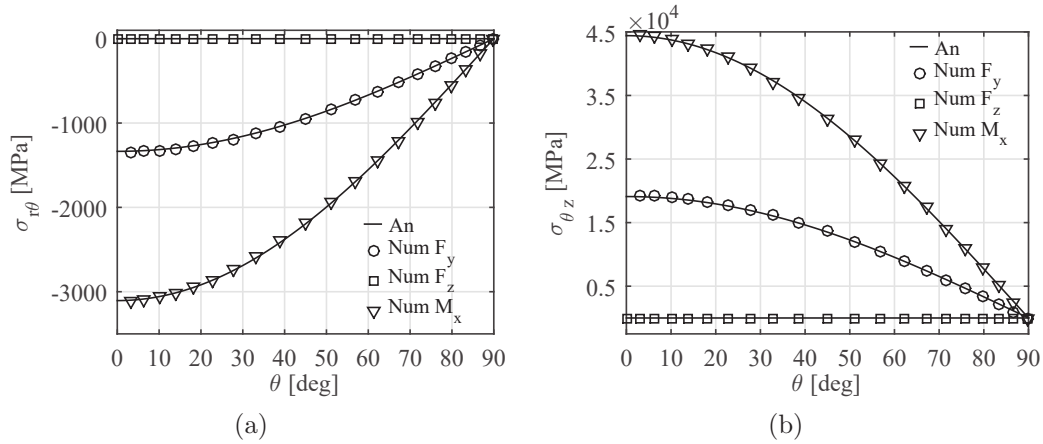

Figure 19: (a) σ_{tz} and (b) σ_{rt} stress distributions along a quarter of a cone.

one shown in Fig. 21: the analytical solution derived in Section 2 is still valid and only the stress components which are function of $\sin\alpha$ and $\tan\alpha$ change when the taper is negative. The variables of this study are chosen as the taper angle, $\alpha \in [-15\,\mathrm{deg}; 15\,\mathrm{deg}]$, and the eccentricity parameter $e \in [-15\,\mathrm{m}; 15\,\mathrm{m}]$. Furthermore, the von Mises criterion, here employed in cylindrical coordinates, is used to evaluate the variation of the number of cycles in fatigue, when the taper effects are not neglected. The number of cycles to failure N can be determined by employing the well-known Basquin
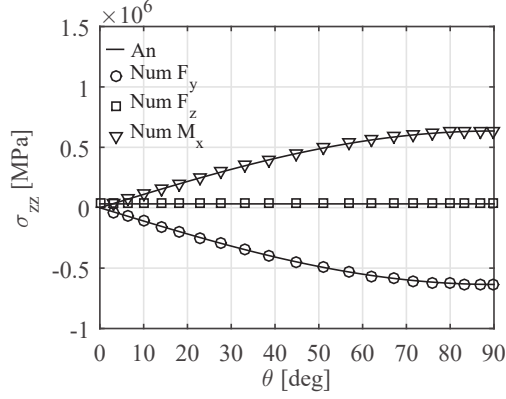
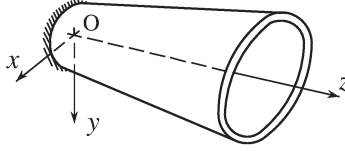Figure 20: σ_{zz} stress distribution along a quarter of a cone.

Figure 21: Conical cantilever beam tapered by a constant negative angle, $\alpha \in [0 \text{ deg}; 15 \text{ deg}]$.

law [33]. The material used in this study is steel, whose Basquin's constants, defined from the ultimate tensile strength and the endurance limit of the material, are $C = 4.56 \times 10^{30}$, and $n = -9.84$ [34].

4.2.1. Von Mises stress

The von Mises stresses were evaluated along the control cross section for $0 \leq \theta \leq \pi/2$, and the maximum stress was subsequently normalised with the maximum von Mises stress in the cylindrical beam.

Figure 22 (a) shows the variation of the normalised von Mises stresses within the eccentricity for two different taper angles, 0.5 deg, 15 deg. Four zones are highlighted in the legend. Zone 1 presents constant lines: the von Mises stresses are not a function of the eccentricity and they increase quadratically with the taper angle, as shown by the continuous line in Fig. 22 (b). In zone 2 only negative eccentricities are involved and the von Mises stresses augment when $e \to 0$. The sensitivity of the von Mises stress towards the eccentricity is proportional to the taper angle. The dashed line in Fig. 22 (b) shows that in a cone with a taper angle of $\alpha = 15$ deg, an eccentricity
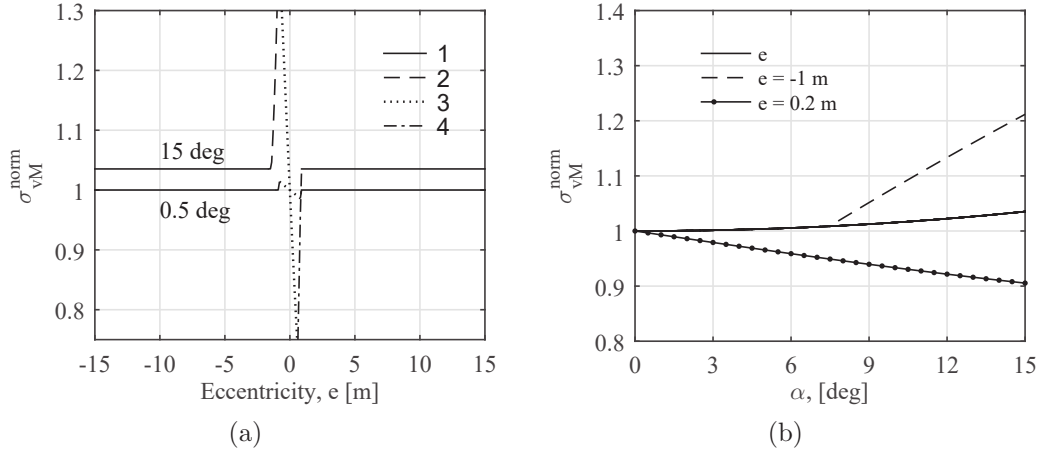
24

Figure 22: (a) Normalised von Mises stresses variation (conical over cylindrical) with eccentricity for different taper angles; (b) Normalised von Mises stresses variation (conical over cylindrical) with α for different eccentricities.

$e = -1\,$m causes an increase of 20% of the equivalent stress. Between zone 2 and zone 3 a local maximum occurs. Zone 3 includes positive and negative eccentricities and in here the equivalent stresses decrease to a local minimum at $e = 0.5\,$m. In the range $0 \leq e \leq 0.5\,$m, the taper reduces the von Mises stress in the cylinder, as shown by the point-dashed line in Fig. 22 (b). Finally, in zone 4 the von Mises stresses increase again.

4.2.2. Fatigue life

The aforementioned maximum equivalent stresses were employed to investigate the relation between the taper angle variation and the fatigue behaviour. In this case, the number of cycles to failure was evaluated for the set of cones previously defined and then normalised to the number of cycles to failure in the respective cylindrical beam. Since the number of cycles to failure is inversely proportional to the equivalent stress [33], in Fig. 23 (a) the same four zones can be distinguished. Zone 1 is not a function of the eccentricity and the normalised number of cycles decreases with the increase of the taper, as shown by the continuous line in Fig. 23 (b). Zone 2 extends in the negative eccentricities and presents a decrement of $\tilde{N}$ with the eccentricity. As expected, the smaller the taper is, the smaller the eccentricity has to be to affect $\tilde{N}$. For example, in Fig. 23 (b), for $e = -0.2\,$m and $\alpha = 5$ deg, $\tilde{N}$ decreases already of approximately 10%. In zone 3, $\tilde{N}$ moves
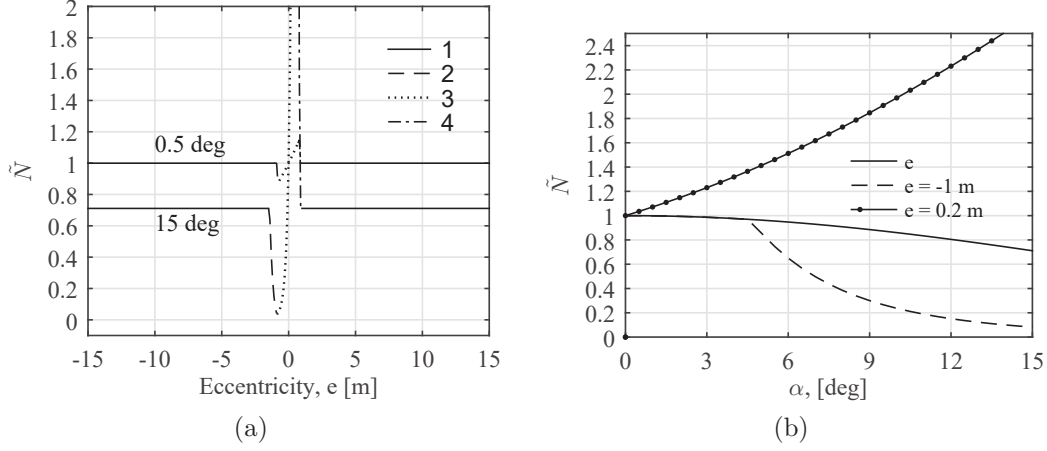
Figure 23: (a) Normalised number of cycles to failure variation with the eccentricity for different taper angles; (b) normalised number of cycles to failure variation with the taper angle for different eccentricities.

from a local minimum in the negative eccentricity zone, to a local maximum at $e = 0.5$ m. In the range $0 \leq e \leq 0.5$ m the number of cycles to failure significantly increases. Figure 23 (b) shows that $\tilde{N}$ doubles when $e = 0.2$ m and $\alpha = 5$ deg. Finally, $\tilde{N}$ decreases in zone 4 .

4.2.3. Negative taper

Lastly, the effects of the sign of the taper on the maximum equivalent stress that occur in a cross section of a conical beam were studied. The normalised parameter σ_{vM}^{α} was defined as ratio between the maximum von Mises stress in a negatively and a positively tapered beam. In Fig. 24 (a) the variation of the equivalent stress with the eccentricity is shown for $\alpha = \pm 0.5$ deg and $\alpha = \pm 15$ deg and four different zones are distinguished in the legend. In zone 1, the sign of the taper does not affect the maximum von Mises stress. Zone 2 extends in the negative eccentricities. In here, a positive taper causes a higher stress than the same negative taper. For example, Fig. 24 (b) shows that for $e = 0.5$ m, a taper $\alpha = 5$ deg produces a von Mises stress 20% higher than $\alpha = -5$ deg. Furthermore, the less pronounced the taper is, the smaller the eccentricity has to be to have the sign affecting the equivalent stress. Zone 3 extends from the local maximum in the negative eccentricities to the local minimum in the positive eccentricities, passing by $\sigma_{vM}^{\alpha} = 1$ where the eccentricity is zero. Negative tapers have a worst effect
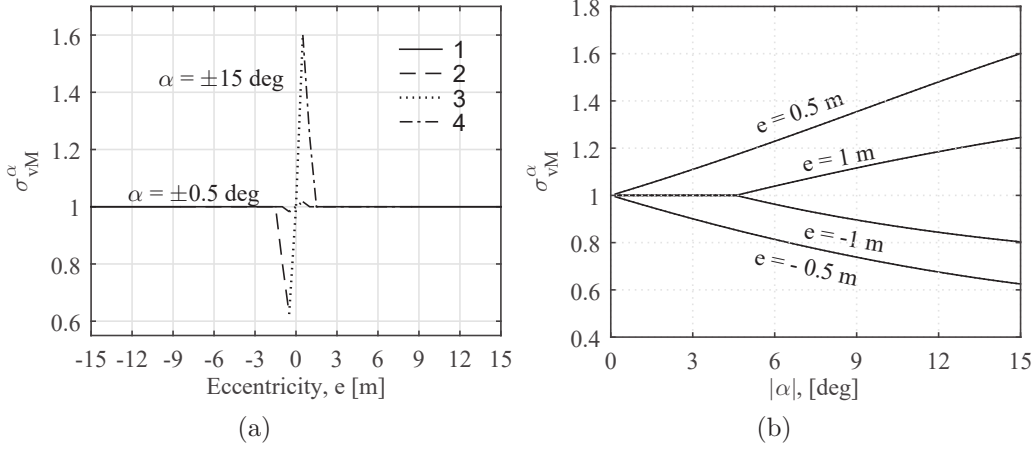
26

Figure 24: The parameter σ_{vM}^{α} shows the effects of negative α in comparison with positive α. (a) Its variation with α is shown for different eccentricities; (b) Its variation with e is shown for different α.

when positive eccentricities occur. Zone 4 has the same properties as zone 2, but it refers to positive eccentricities and negative tapers.

5. Discussion

Although the analytical solutions presented in this article are an approximation due to the adoption of Navier's equation (i.e. strictly speaking Navier does not hold in tapered cross-sections), good agreement was found between the analytically and numerically predicted stress components. It is noteworthy that the validity of the provided solutions is restricted to moderately tapered cross sections in sufficiently slender beams where the axial stress component σ_{zz} follows a quasi-linear distribution.

In the case of the vertically tapered box beam, all six Cauchy stress components are induced in the flange. Figure 13 a shows the σ_{xx} parabolic distribution with zero magnitude at the corners i.e. $x = \pm b$, and maximum at $x = 0$: shear load and bending result in a concave distribution whereas axial loading causes a convex distribution. The σ_{zz} component is not a function of the taper angle, therefore it has the same distribution as in a classic prismatic beam. Interestingly, the components σ_{yz} and σ_{yy} in the flange are proportional to the σ_{zz} component and has, therefore, a constant distribution, as shown in Figs. 14. In Figure 15 b, the component σ_{xz} is not only induced by the shear load, as in a prismatic beam, but also by bending

27

moment and axial load. In all cases, the stress exhibits a linear distribution with a zero transition at $x = 0$. The in-plane shear stress component σ_{xy} in in Fig. 15 a presents a similar behaviour. It is worth noting that the maximum stress varies with the sign of the applied forces. In the web of a vertically tapered beam it was found that only the components σ_{zz}, σ_{yz} and σ_{yy} are non-zero. The normal stress in Fig. 15 a has the same linear distribution as evident in the prismatic case. The out-of-plane shear stress component σ_{yz} in Fig. 15 b, follows a quadratic distribution under shear load and bending moment, and a linear distribution under axial load. In a tapered beam under shear load, σ_{yz} follows the classic concave quadratic distribution, with its maximum at $y = 0$; conversely, the application of a bending moment can result in a convex stress distribution. In the latter case, it is possible that the shear stress distribution attains its maximum at $y = \pm h$. Figure 15 shows that the axial and shear loads induce a convex quadratic σ_{yy} distribution whereas bending causes a concave cubic stress distribution.

In the case of a conical beam only the hoop stress component $\sigma_{\theta\theta}$ is zero. The axial stress component σ_{zz} in a conical has the same distribution than in a cylindrical beam as stipulated in the derivation. Both the shear stress σ_{zr} and the through thickness σ_{rr} in Fig. 18 are proportional to the axial stress component σ_{zz}. In contrast to the cylindrical beam, the shear stress $\sigma_{z\theta}$, and $\sigma_{r\theta}$, are functions of all the three cross section forces. Their distributions are trigonometric and both of which attain their maximum at $\theta = 0$ and their zero values at $\theta = \pm \pi/2$, as shown in Fig. 19.

The parametric study shows that neglecting the taper leads to an over- or underestimation of the stresses in the cross section. The equivalent stress always increases when a cylindrical beam is tapered, except in the range $0 < e < 0.5$ m, as shown in Fig. 19 a. As previously mentioned, the study is based on the comparison between the maximum equivalent stress that occurs in a conical beam and the one in a cylindrical beam. It is important to highlight that, when the eccentricity approaches zero, the maximum von Mises stresses occur at different locations of the cross sections in the cylindrical beam and in the cone, resulting in the four behaviours of the equivalent stress ratio highlighted in Fig. 22. In zone 1, the maximum von Mises stress occurs at $\theta = 90$ deg; consequently, in the set of Eqs. (35) - (43) all the terms which are multiplied by $\cos\theta$ vanish, and the ratio of the equivalent stresses between cone and cylinder are no longer a function of the eccentricity. In zone 2, the maximum equivalent stress occurs at $\theta = 0$ deg in the conical beams and $\theta = 90$ deg in the cylinder for negative e; otherwise for positive e. Lastly,

the drop in zone 3 is caused by the maximum equivalent stress occurring at $\theta = 0$ deg in both conical and cylindrical beams. The maximum von Mises stress moves from $\theta = 90$ deg to $\theta = 0$ deg in zone 4.

Eventually it can be concluded that neglecting the taper effects leads to an overestimation of the number of cycles to failure, except for the known range $0 \leq e \leq 0.5$ m. When a conical beam has a negative taper, both $\sigma_{r\theta}$ and $\sigma_{z\theta}$ are affected since they are functions of $\sin\theta$. The sign of the taper, together with the loading direction leads to critical designs. In particular, when a negative eccentricity is applied, a negative taper halves the equivalent stress caused by the equivalent positive taper; vice-versa when a positive eccentricity is applied. Nonetheless, the equivalent stress is not affected by the orientation of the taper in zone 1.

6. Conclusions

The following conclusions can be drawn from the analytical stress solutions and the parametric studies conducted:

i The introduction of taper into beams can potentially evoke all six stress components already at seemingly small taper angles.

ii In principle all three cross section forces are highly coupled to the stress components in tapered beams. That is to say, a decoupling of shear force from bending and axial force as in prismatic beams is not per-se admissible in tapered beams.

iii Application of prismatic solutions such as Jourawski's shear stress formula to tapered beams can lead to results which are significantly at variance with the real stress states. In contrast to the widely and erroneously established assumption in engineering practice, the stress state in tapered beams cannot be obtained by pure stress tensor transformation of the prismatic solution into a local coordinate system.

iv Ignoring the taper can lead to an underestimation of the von Mises stress representing a non-conservative assumption. In the present study of a conical cantilever beam – considering static loading conditions – the von Mises stress increased less than 1% for $\alpha \leq 8$ deg and exceeded 10% for $\alpha \geq 25$ deg.

v Ignoring the taper can lead to a significant overestimation of the fatigue life. In the present study of a conical beam the number of cycles to failure decreased by 10% for $\alpha = 5$ deg and decreased by 40% for $\alpha = 25$ deg.

vi The analytical solutions and the parametric study in this article were based on isotropic material properties. However, it is deemed that additional stress components similarly to those presented will also be evoked in tapered beams with anisotropic material behaviour, such as fibre reinforced composites. Bearing in mind that composite materials are highly susceptible to failure owing to inter-fibre stress components, emphasises the importance of an accurate prediction of the stress components especially in tapered beams.

Possible future developments of the present work include the derivation of closed-form solutions in terms of strains and displacements for the analysed cases, as well as the solution for stresses in horizontally tapered and doubly tapered box girders. Moreover, the extended Jourawski's formula could be further extended to beams with non-symmetric or non-homogeneous (e.g. laminated) cross sections.

Acknowledgements

References

[1] W. McGuire, G. Winter, Steel Structures, Prentice-Hall, Englewood Cliffs, 1968.

[2] D. Peery, Aircraft Structures, McGraw-Hill, New York, 1950.

[3] E. Hau, Wind turbines: fundamentals, technologies, application, economics, 3rd Edition, Springer, New York, 2013.

[4] S. Bennati, P. Bertolini, L. Taglialegne, P. S. Valvo, On stresses in tapered beams, Meccanica(submitted).

[5] G. Balduzzi, G. Hochreiner, J. Füssl, Stress recovery from one dimensional models for tapered bi-symmetric thin-walled I beams: Deficiencies in modern engineering tools and procedure, Thin-Walled Structures 119 (1) (2017) 934–944.

[6] L. Taglialegne, Stress fields in wind turbine blades with thin-walled variable cross sections, Ph.D. thesis, International Doctorate "Civil and Environmental Engineering", Universities of Florence, Perugia and Pisa – TU C.W. Braunschweig (2018).

[7] S. Timoshenko, Bending stresses in curved tubes of rectangular cross section, Transactions of the American Society of Mechanical Engineers 45 (1923) 135–140.

[8] F. Bleich, Stahlhochbauten, Vol. 1, Berlin: Springer, 1932, Language: German.

[9] A. Paglietti, G. Carta, Remarks on the current theory of shear strength of variable depth beams, Open Civil Engineering Journal 3 (1) (2009) 28–33.

[10] E. H. Atkin, Tapered beams: suggested solutions for some typical aircraft cases (Parts I & II), Aircraft Engineering and Aerospace Technology 10 (11) (1938) 347–351.

[11] E. H. Atkin, Tapered beams: suggested solutions for some typical aircraft cases (Part III), Aircraft Engineering and Aerospace Technology 10 (12) (1938) 371–374.

[12] J. L. Krahula, Shear formula for beams of variable cross section, AIAA Journal 13 (10) (1975) 1390–1391.

[13] S. P. Timoshenko, J. M. Gere, Mechanics of Materials, Van Nostrand Reinhold, New York, 1972.

[14] R. J. Knops, P. Villaggio, Recovery of stresses in a beam from those in a cone, Journal of Elasticity 53 (1999) 65–75.

[15] N. S. Trahair, P. Ansourian, In-plane behaviour of web-tapered beams, Engineering Structures 108 (2016) 47–52.

[16] G. Lee, B. Szabo, Torsional response of tapered I-girders, Journal of the Structural Division 93 (5) (1967) 233–252.

[17] G. Lee, M. Morrell, R. L. Ketter, Design of tapered members, Welding Research Council Bulletin (173) (1972) 1–32.

[18] K. Chong, W. Swanson, R. Matlock, Shear analysis of tapered beams, Journal of the Structural Division 102 (9) (1976) 1781–1788.

[19] D. H. Hodges, J. C. Ho, W. Yu, The effect of taper on section constants for in-plane deformation of an isotropic strip, Journal of Mechanics of Materials and Structures 3 (3) (2008) 425–440.

[20] D. H. Hodges, A. Rajagopal, J. C. Ho, W. Yu, Stress and strain recovery for the in-plane deformation of an isotropic tapered strip-beam, Journal of Mechanics of Materials and Structures 5 (6) (2010) 963–975.

[21] A. Rajagopal, Advancements in rotor blade cross-sectional analysis using the variational-asymptotic method, Ph.D. thesis, Georgia Institute of Technology (2014).

[22] G. Balduzzi, M. Aminbaghai, E. Sacco, J. Füssl, J. Eberhardsteiner, F. Auricchio, Non-prismatic beams: a simple and effective timoshenko-like model, International Journal of Solids and Structures 90 (2016) 236–250.

[23] G. Balduzzi, M. Amindaghai, F. Auricchio, J. Füssl, Planar Timoshenko-like model for multilayer non-prismatic beams, International Journal of Mechanics and Materials in Design 14 (1) (2018) 51–70.

[24] J. Michell, The stress in an æolotrophic elastic solid with an infinite plane boundary, Proceedings of the London Mathematical Society s1-32 (1) (1900) 247–257.

[25] S. Carothers, Plane strain in a wedge, with applications to masonry dams, Proceedings of the Royal Society of Edinburgh 33 (1914) 292–306.

[26] S. Bennati, P. Bertolini, L. Taglialegne, P. S. Valvo, On shear stresses in tapered beams, in: Proceedings of the GIMC-GMA 2016 - 21st Italian Conference on Computational Mechanics and 8th Meeting of the AIMETA Materials Group, Lucca, 2016.

[27] J. P. Blasques, Users manual for BECAS a cross section analysis tool for anisotropic and inhomogeneous beam sections of arbitrary geometry, Tech. rep., DTU Wind Energy, Technical University of Denmark, Roskilde (2012).

[28] C. E. Cesnik, D. H. Hodges, VABS: a new concept for composite rotor blade cross-sectional modeling, Journal of the American helicopter society 42 (1) (1997) 27–38.

[29] B. A. Boley, On the accuracy of the bernoulli-euler theory for beams of variable section, Journal of applied mechanics 30 (3) (1963) 373–378.

[30] S. Timoshenko, J. N. Goodier, Theory of Elasticity, McGraw-Hill book Company, 1951.

[31] ABAQUS 2017, Documentation, Dassault Systemes Simulia Corporation.

[32] A. A. Poli, M. C. Cirillo, On the use of the normalized mean square error in evaluating dispersion model performance, Atmospheric Environment. Part A. General Topics 27 (15) (1993) 2427–2434.

[33] O. H. Basquin, The exponential law of endurance tests, American Society of Testing Materials 10 (1910) 625–630.

[34] C. Li, W. Dai, F. Duan, Y. Zhang, D. He, Fatigue life estimation of medium-carbon steel with different surface roughness, Applied Sciences 7 (4) (2017) 338.

Appendix A. Cauchy's equilibrium equations in Cartesian coordinates

The well-known Cauchy's differential equations expressing local equilibrium in Cartesian coordinates are [30]:

$$\frac{\partial \sigma_{xx}}{\partial x} + \frac{\partial \sigma_{xy}}{\partial y} + \frac{\partial \sigma_{xz}}{\partial z} = 0 \tag{A.1}$$

$$\frac{\partial \sigma_{yx}}{\partial x} + \frac{\partial \sigma_{yy}}{\partial y} + \frac{\partial \sigma_{yz}}{\partial z} = 0 \tag{A.2}$$

$$\frac{\partial \sigma_{zz}}{\partial x} + \frac{\sigma_{zy}}{\partial y} + \frac{\sigma_{zz}}{\partial z} = 0 \tag{A.3}$$

Appendix B. Cauchy equilibrium equations for a thin-walled conical element

The volume of an infinitesimally small thin-walled cone element (Fig. B.25) can be obtained – under consideration of small angles $\mathrm{d}\theta$ – by the trapezoidal equation as follows:

$$\mathrm{d}V = \frac{1}{2}t_f \left[r\,\mathrm{d}\theta + (r + \mathrm{d}r)\,\mathrm{d}\theta \right] \frac{\mathrm{d}z}{\cos\alpha} = r\,t_p\,\mathrm{d}\theta\,\mathrm{d}z \tag{B.1}$$

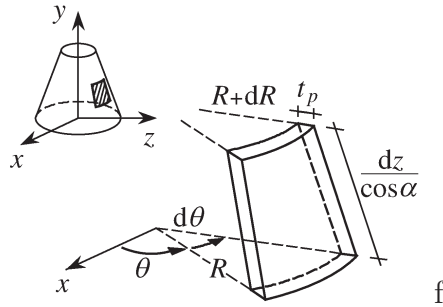

Figure B.25: Infinitesimally small element of a thin-walled cone.

Translatory equilibrium is imposed in the three main directions as follows. In the r direction:

$$- \sigma_{rz}\, r\, t_p\, \mathrm{d}\theta + (\sigma_{rz} + \mathrm{d}\sigma_{rz})\, (r + \mathrm{d}r)\, t_p\, \mathrm{d}\theta$$

$$- (\sigma_{\theta\theta} + \mathrm{d}\sigma_{\theta\theta})\, t_p \sin\frac{\mathrm{d}\theta}{2}\, \mathrm{d}z + (\sigma_{r\theta} + \mathrm{d}\sigma_{r\theta})\, t_p \cos\frac{\mathrm{d}\theta}{2}\, \mathrm{d}z$$

$$- \sigma_{\theta\theta} t_p \sin\frac{\mathrm{d}\theta}{2}\, \mathrm{d}z - \sigma_{r\theta} t_p \cos\frac{\mathrm{d}\theta}{2}\, \mathrm{d}z + b_r r\, t_p\, \mathrm{d}\theta\, \mathrm{d}z = 0 \qquad \text{(B.2)}$$

In θ direction:

$$- \sigma_{\theta\theta}\, t_p \cos\frac{\mathrm{d}\theta}{2}\, \mathrm{d}z + \sigma_{r\theta}\, t_p \sin\frac{\mathrm{d}\theta}{2}\, \mathrm{d}z + (\sigma_{\theta\theta} + \mathrm{d}\sigma_{\theta\theta})\, t_p \cos\frac{\mathrm{d}\theta}{2}\, \mathrm{d}z - \sigma_{\theta z} r\, t_p\, \mathrm{d}\theta$$

$$+ (\sigma_{r\theta} + \mathrm{d}\sigma_{r\theta})\, t_p \sin\frac{\mathrm{d}\theta}{2}\, \mathrm{d}z + (\sigma_{\theta z} + \mathrm{d}\sigma_{\theta z})\, (r + \mathrm{d}r)\, t_p\, \mathrm{d}\theta + b_\theta\, r\, t_p\, \mathrm{d}\theta\, \mathrm{d}z = 0$$

$$\text{(B.3)}$$

In z direction:

$$- \sigma_{zz} r t_p\, \mathrm{d}\theta + (\sigma_{zz} + \mathrm{d}\sigma_{zz})\, (r + \mathrm{d}r)\, t_p\, \mathrm{d}\theta$$

$$- \sigma_{\theta z}\, t_p\, \mathrm{d}z + (\sigma_{\theta z} + \mathrm{d}\sigma_{\theta z})\, t_p\, \mathrm{d}z + b_z\, r\, t_p\, \mathrm{d}\theta\, \mathrm{d}z = 0 \qquad \text{(B.4)}$$

After some manipulation of the set of Eqs. (B.2), (B.4) and by using Eq. (B.1) the Cauchy equilibrium equations for a conical beam in cylindrical coordinates are the following:

$$\frac{1}{R}\left(-\sigma_{\theta\theta} + \sigma_{rz}\frac{\mathrm{d}R}{\mathrm{d}z} + \frac{\partial\sigma_{r\theta}}{\partial\theta}\right) + \frac{\partial\sigma_{rz}}{\partial z} + b_r = 0 \qquad \text{(B.5)}$$

$$\frac{1}{R}\left(\sigma_{r\theta} + \sigma_{\theta z}\frac{\mathrm{d}R}{\mathrm{d}z} + \frac{\partial\sigma_{\theta\theta}}{\partial\theta}\right) + \frac{\partial\sigma_{\theta z}}{\partial z} + b_\theta = 0 \qquad \text{(B.6)}$$

$$\frac{1}{R}\left(\sigma_{zz}\frac{\mathrm{d}R}{\mathrm{d}z} + \frac{\partial\sigma_{\theta z}}{\partial\theta}\right) + \frac{\partial\sigma_{zz}}{\partial z} + b_z = 0 \qquad \text{(B.7)}$$